Supplementary Information

Interpretable Classification of Time Series Using Euler Characteristic Surfaces

Buddha Nath Sharma, Vishal Mandal, Salam Rabindrajit Luwang, Md. Nurujjaman,

Atish J. Mitra, Sushovan Majhi

Contents

1 Geometric Constructions: Voronoi Cells, Nerve, and Alpha Complex

This section provides geometric illustrations and formal definitions of the Voronoi diagram, the nerve (Čech complex), and the Alpha complex—the building blocks of our topological pipeline.

Formal definitions. Given a collection of subsets $\mathcal{U} = \{U_\alpha\}_{\alpha \in \Lambda}$ of a topological space, the *nerve* of $\mathcal{U}$ is the simplicial complex $N(\mathcal{U})$ whose vertex set is Λ, and where a subset $\{\alpha_0, \alpha_1, \ldots, \alpha_k\} \subseteq \Lambda$ spans a k-simplex if and only if $U_{\alpha_0} \cap U_{\alpha_1} \cap \cdots \cap U_{\alpha_k} \neq \emptyset$.

For a dataset $P = \{x_1, x_2, \ldots, x_n\} \subset \mathbb{R}^d$ and closed ball $B(x_i, r)$, the *Čech complex* at scale r is:

$$C(P, r) = \left\{ \sigma \subset P : \bigcap_{x_i \in \sigma} B(x_i, r) \neq \emptyset \right\}.$$

The *Voronoi cell* for $x_i \in P$ is $V(x_i) = \{x \in \mathbb{R}^d \mid d(x, x_i) \leq d(x, x_j),\ \forall x_j \in P\}$. The *Alpha complex* at scale r is the nerve of the collection $\{V(x_i) \cap B(x_i, r)\}_{x_i \in P}$ [1].

Illustration. We consider six points forming a regular hexagon:

$$S = \{(0, 2), (2, 1), (2, -1), (0, -2), (-2, -1), (-2, 1)\}.$$

Figure S1 shows the Voronoi cells, the Čech complex (nerve), and the Alpha complex for this dataset. In Fig S1 (a), green dotted lines divide the space into six Voronoi regions. In Fig S1 (b), the Čech complex at a fixed radius includes all edges and triangles wherever corresponding balls mutually intersect. In Fig S1 (c), the Alpha complex restricts the Čech complex to simplices consistent with the Voronoi decomposition, yielding a sparser complex that still captures the essential topology.

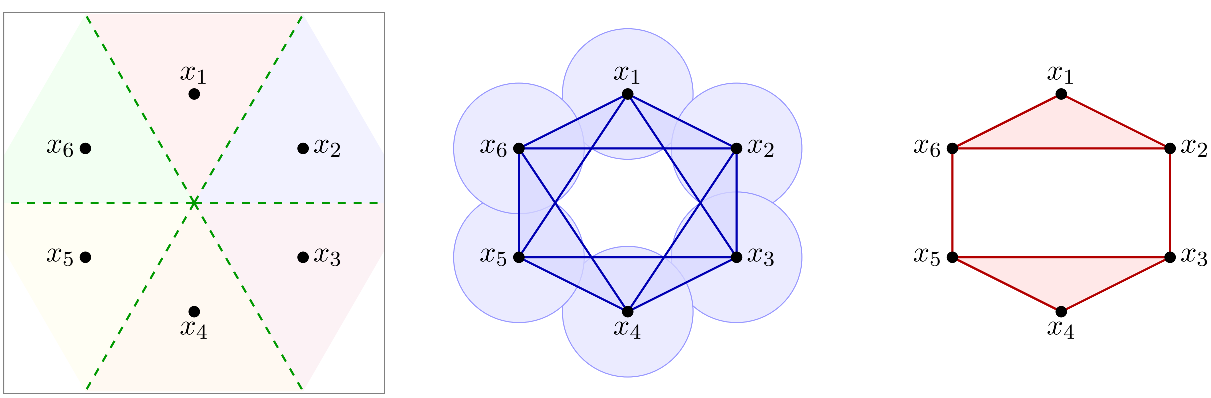

Figure S1: Illustration of the (a) Voronoi diagram, (b) Nerve (Čech complex), and (c) Alpha complex for the hexagonal point set S.

2 Classification Flowcharts

Single-Feature Threshold Classifier

The flowchart in Fig. S2 illustrates the complete workflow of the single-feature ECS-based classification framework described in the Methods section of the main manuscript.

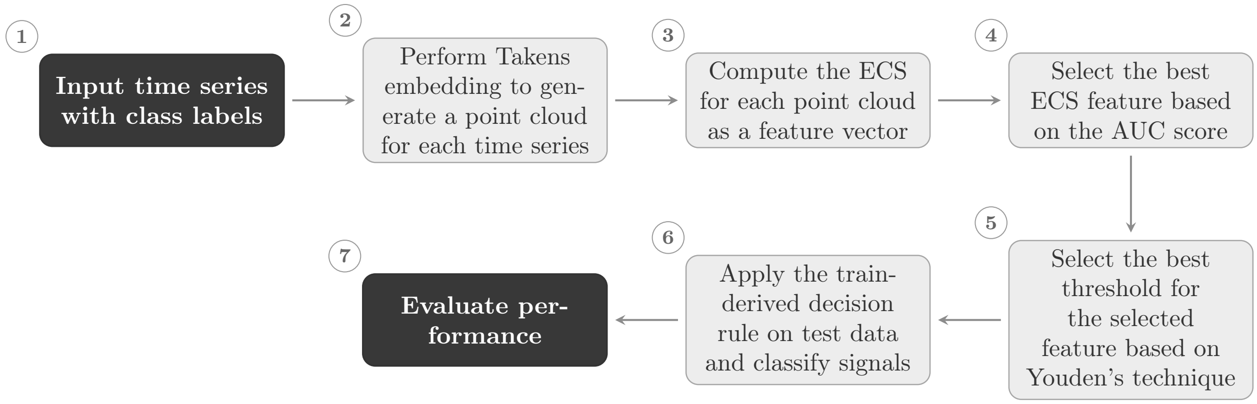

Figure S2: Flowchart of the ECS-based single-feature threshold classification framework.

AdaBoost Ensemble Classifier

The flowchart in Fig. S3 illustrates the complete workflow of the ECS-based AdaBoost classification framework.

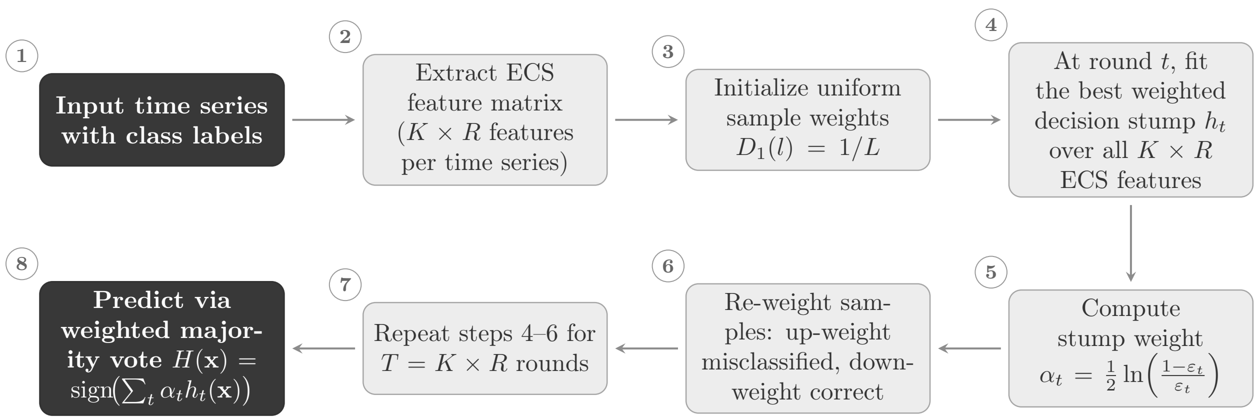

Figure S3: Flowchart of the ECS-based AdaBoost classification framework. The number of weak learners T is set equal to $K \times R$, matching the dimensionality of the ECS feature vector.

3 Proof of Stability Results

This section provides full proof of Lemma S1 stated in the main manuscript (therein referred to as Lemma 1). We first recall the relevant background from algebraic topology.

Betti numbers and Euler characteristic. Using homology of a simplicial complex $\mathcal{K}$, an equivalent definition of its Euler characteristic is:

$$\chi(\mathcal{K}) = \sum_{i=0}^{\dim(\mathcal{K})} (-1)^i \, \beta_i(\mathcal{K}), \tag{S1}$$

where β_i is the i-th Betti number of $\mathcal{K}$ [2].

Persistence diagrams and Wasserstein distance. The *persistence diagram* $\mathrm{PD}_n(\mathcal{K})$ of a filtration $\mathcal{K}_0 \subseteq \mathcal{K}_1 \subseteq \cdots \subseteq \mathcal{K}_s$ and homological degree n is the multiset of points $(a_i, a_j) \in \overline{\mathbb{R}}^2$ with $i < j$, each assigned a nonzero multiplicity $\mu_{i,j}^n$, with points on the diagonal included with infinite multiplicity [3].

For $p \geq 1$, the *degree-p Wasserstein distance* between two persistence diagrams $\mathrm{PD}_n(\mathcal{K})$ and $\mathrm{PD}_n(\mathcal{L})$ is:

$$W_p(\mathrm{PD}_n(\mathcal{K}), \mathrm{PD}_n(\mathcal{L})) := \inf_{\varphi} \left(\sum_{x \in \mathrm{PD}_n(\mathcal{K})} d\big(x, \varphi(x)\big)^p \right)^{1/p},$$

where φ is a bijection from $\mathrm{PD}_n(\mathcal{K})$ to $\mathrm{PD}_n(\mathcal{L})$.

Lemma S1 (Stability of Alpha Filtrations in $\mathbb{R}^3$)**.** *Let $\mathcal{D} = \{x_1, \ldots, x_M\}$ be a point cloud in $\mathbb{R}^3$. Then, for an arbitrary small $0 < \epsilon < \frac{1}{2}\min_{1\leq i<j\leq M}\|x_i - x_j\|_2$, there is $\delta > 0$ such that for any $\mathcal{D}' = \{x_1', \ldots, x_M'\}$ with $\max_{1\leq i\leq M} \|x_i - x_i'\|_2 \leq \delta$,*

$$\|\chi(\mathcal{K}(r)) - \chi(\mathcal{K}'(r))\|_1 \leq \frac{1}{4}M^4\epsilon,$$

where $\mathcal{K}(r)$ and $\mathcal{K}'(r)$ are the corresponding Alpha filtrations on $\mathcal{D}$ and $\mathcal{D}'$, respectively.

Proof. We note that for any non-degenerate simplex (triangle or tetrahedron) T in $\mathbb{R}^3$ and for any $\epsilon > 0$, there is a $\delta_T > 0$ such that after perturbing the vertices by δ_T, the circumradius of T is changed by at most ϵ (this follows from the continuity of the circumradius function of a non-degenerate simplex).

Let $\epsilon > 0$ be less than $\frac{1}{2}\min_{1\leq i\neq j\leq M} \|x_i - x_j\|_2$. Choose $\delta > 0$ such that for $x_i' \in \mathcal{D}'$ we have $\|x_i' - x_i\| < \min_T \delta_T$, where the minimum is over all non-degenerate simplices formed by points of $\mathcal{D}$. Take the filtering function on a simplex in [4, Theorem 2] to be the radius of the smallest enclosing sphere of the points defining the simplex, with f corresponding to points in $\mathcal{D}$ and g corresponding to points in $\mathcal{D}'$.

Then, by the Cellular Wasserstein theorem of Skraba and Turner, we have for $n = 0, 1, 2$ (noting that the smallest enclosing sphere of a finite set of points in $\mathbb{R}^3$ is realized by two, three, or four of those points):

$$W_1(\mathrm{PD}_0(f), \mathrm{PD}_0(g)) \leq \binom{M}{2}\epsilon,$$

$$W_1(\mathrm{PD}_1(f), \mathrm{PD}_1(g)) \leq \binom{M}{2}\epsilon + \binom{M}{3}\epsilon = \binom{M+1}{3}\epsilon,$$

$$W_1(\mathrm{PD}_2(f), \mathrm{PD}_2(g)) \leq \binom{M}{3}\epsilon + \binom{M}{4}\epsilon = \binom{M+1}{4}\epsilon.$$

Finally, from Theorem 1 of [2]:

$$\begin{aligned}\|\chi(\mathcal{K}(r)) - \chi(\mathcal{K}'(r))\|_1 &\leq 2\sum_{n=0}^{2} W_1(\mathrm{PD}_n(\mathcal{K}), \mathrm{PD}_n(\mathcal{K}')) \\ &= 2\left[2\binom{M}{2} + 2\binom{M}{3} + \binom{M}{4}\right]\epsilon \leq \frac{1}{4}M^4\epsilon.\end{aligned}$$

We sum only over $n = 0, 1, 2$ because the Čech filtration has the same persistent homology as the Alpha filtration. ∎

Remark. Since this paper uses Takens embedding dimension $m = 3$ for most datasets, we state the stability result here only for $\mathbb{R}^3$. The argument generalizes to $\mathbb{R}^d$ by summing over homological degrees $n = 0, \ldots, d-1$ in the Wasserstein bound, yielding a bound that depends on $\binom{M+1}{d+1}$ rather than $\binom{M+1}{4}$.

4 Rössler System: Pairwise L_1 Distance Analysis

Figure S4 shows (a) the pointwise absolute difference $|\mathrm{ECS}_{\mathrm{chaotic}} - \mathrm{ECS}_{\mathrm{periodic}}|$ across the scale–time grid for the Rössler system, and (b) a heatmap of pairwise L_1 distances between ECSs computed from 100 noisy realizations at each noise level from 0% to 10% of the signal amplitude. Intra-regime distances (off-diagonal blocks) are markedly smaller than inter-regime distances (diagonal blocks), confirming that the ECS is robust to moderate noise levels and that the L_1 metric can quantitatively differentiate between the periodic ($c = 2.3$) and chaotic ($c = 7.3$) regimes.

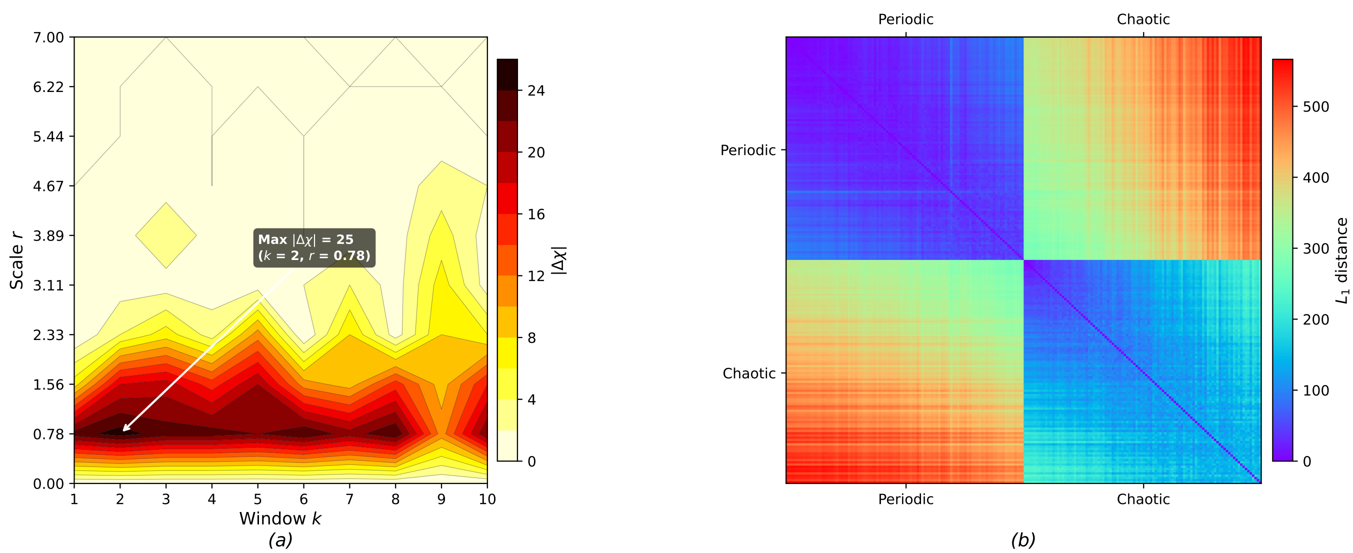

Figure S4: Panel (a) shows the absolute difference $|\mathrm{ECS}_{\mathrm{chaotic}} - \mathrm{ECS}_{\mathrm{periodic}}|$ across the scale–time grid, with the annotated arrow indicating the coordinate of maximum divergence. Panel (b) shows the heatmap of pairwise L_1 distances between ECSs constructed from perturbed time series of the periodic ($c = 2.3$) and chaotic ($c = 7.3$) regimes.

5 ECG5000: Grid Size Optimization and ECS Topological Analysis

Grid Size Optimization

Figure S5 shows the mean cross-validated AUC of the best ECS feature as a function of the ECS grid size K for the *ECG5000* dataset. The AUC rises steeply from a 3×3 grid and reaches a peak at the 10×10 configuration, which was therefore adopted for all single-feature experiments.

Topological Comparison of ECS Representations

Figure S6 (a) shows the point-wise absolute difference $|\Delta\chi|$ between the ECSs of two class shown in Fig.[] ((c) and (d)) of the main manuscript. Fig. S6 (b) shows the pairwise L_1 distance heatmap

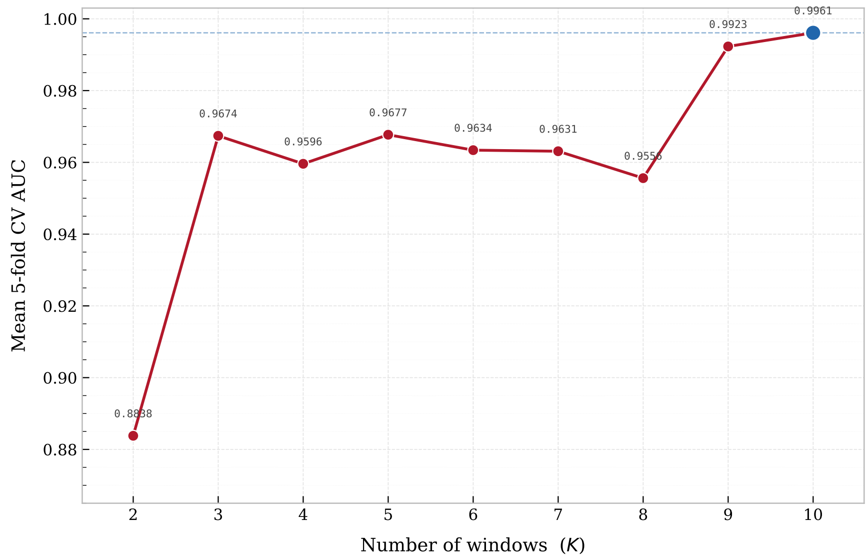

Figure S5: Mean cross-validated AUC of the best ECS feature as a function of the grid size (K) used to construct the ECS for the *ECG5000* dataset.

for all training samples. The higher difference in χ is concentrated at window 8 at scale 0.11, corresponding to scale–time coordinate $(r, t) \approx (0.11, 100)$. The mean intra-class L_1 distances for classes 1 and 2 are 5.58 and 4.14, respectively, while the mean inter-class distance is 8.89, confirming topologically meaningful and class-discriminative information encoded in the ECS.

6 Epilepsy2: ECS Analysis and AdaBoost Contributions

ECS for EEG Signals

Figure S7 shows representative EEG time series and their corresponding ECSs. The seizure ECS (panel (c)) is markedly rougher and more irregular than the smooth, slowly varying non-seizure ECS (panel (d)), reflecting the well-known increase in high-frequency neural oscillations during seizure episodes. This contrast manifests topologically as rapid fluctuations in the connectivity of the Takens point cloud across both scale and time.

Pairwise L_1 Distance Analysis

Figure S8 (a) shows the point-wise absolute difference $|\Delta\chi|$ between the ECSs of the two classes (Fig. S7 (c) and (d)). The differences in χ are spread across multiple windows at scales up to 0.075. Fig. S8 (b) shows the pairwise L_1 distance heatmap between the ECSs constructed from the training samples of the two classes. The pairwise L_1 distances confirm strong inter-class separation. Intra-class distances within the non-seizure class are very small, indicating high topological regularity, while inter-class distances are substantially larger. The higher intra-class separation for the seizure class may be caused by inherent spatiotemporal differences in the EEG signals of different seizure episodes [5].

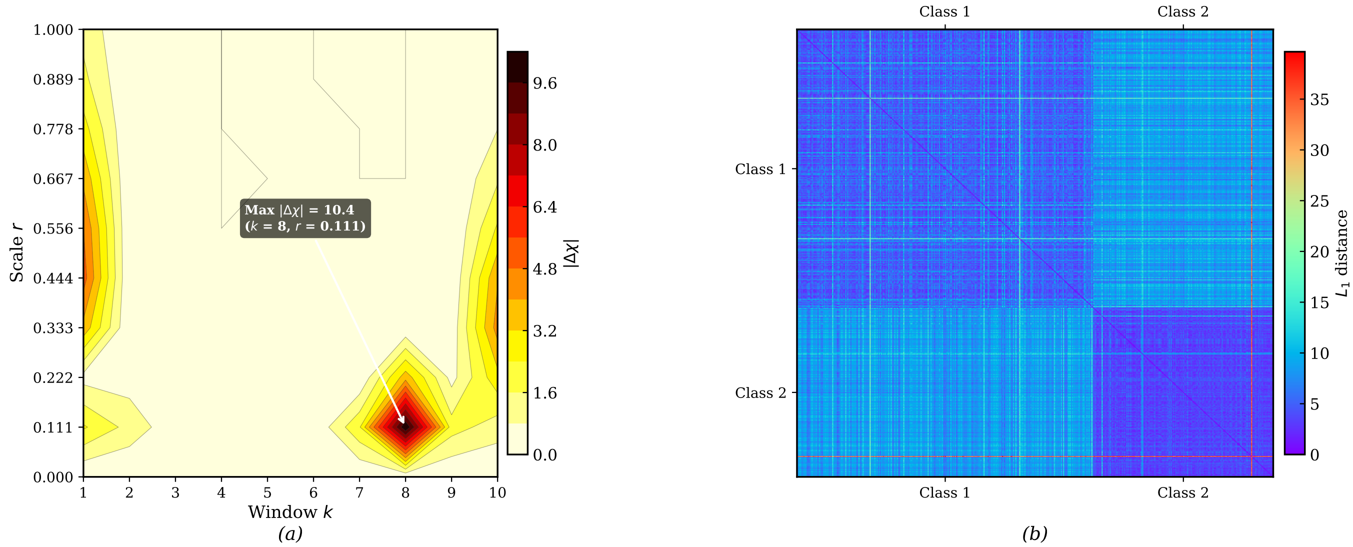

Figure S6: Topological comparison of ECS representations from the *ECG5000* training set. Panel (a) shows the pointwise absolute difference $|\Delta\chi|$ between the ECSs of each class over the scale–window grid. Panel (b) shows the pairwise L_1 distances between the ECSs of all training samples, visualized as a heatmap.

AdaBoost α-Contribution Heatmap

Figure S9 shows the α-contribution heatmap for the AdaBoost ensemble trained on *Epilepsy2*. Unlike in the *ECG5000* case, where a single feature dominates, the *Epilepsy2* heatmap reveals multiple features across temporal blocks that contribute substantially to classification. This demonstrates that when discriminatory information is spread across the spatiotemporal range of the ECS rather than concentrated at a single coordinate, the AdaBoost ensemble effectively combines individually weak stumps into a strong classifier.

References

[1] Edelsbrunner, Letscher, and Zomorodian. Topological persistence and simplification. *Discrete & computational geometry*, 28(4):511–533, 2002.

[2] Anamika Roy, Atish J Mitra, and Tapati Dutta. Euler characteristic surfaces: A stable multiscale topological summary of time series data. *La Matematica*, pages 1–29, 2025.

[3] Nina Otter, Mason A Porter, Ulrike Tillmann, Peter Grindrod, and Heather A Harrington. A roadmap for the computation of persistent homology. *EPJ Data Science*, 6(1):17, 2017.

[4] Primoz Skraba and Katharine Turner. Wasserstein stability for persistence diagrams. *arXiv preprint arXiv:2006.16824*, 2020.

[5] Mariella Panagiotopoulou, Christoforos A. Papasavvas, Gabrielle M. Schroeder, Rhys H. Thomas, Peter N. Taylor, and Yujiang Wang. Fluctuations in eeg band power at subject-specific timescales over minutes to days explain changes in seizure evolutions. *Human Brain Mapping*, 43(8):2460–2477, 2022.

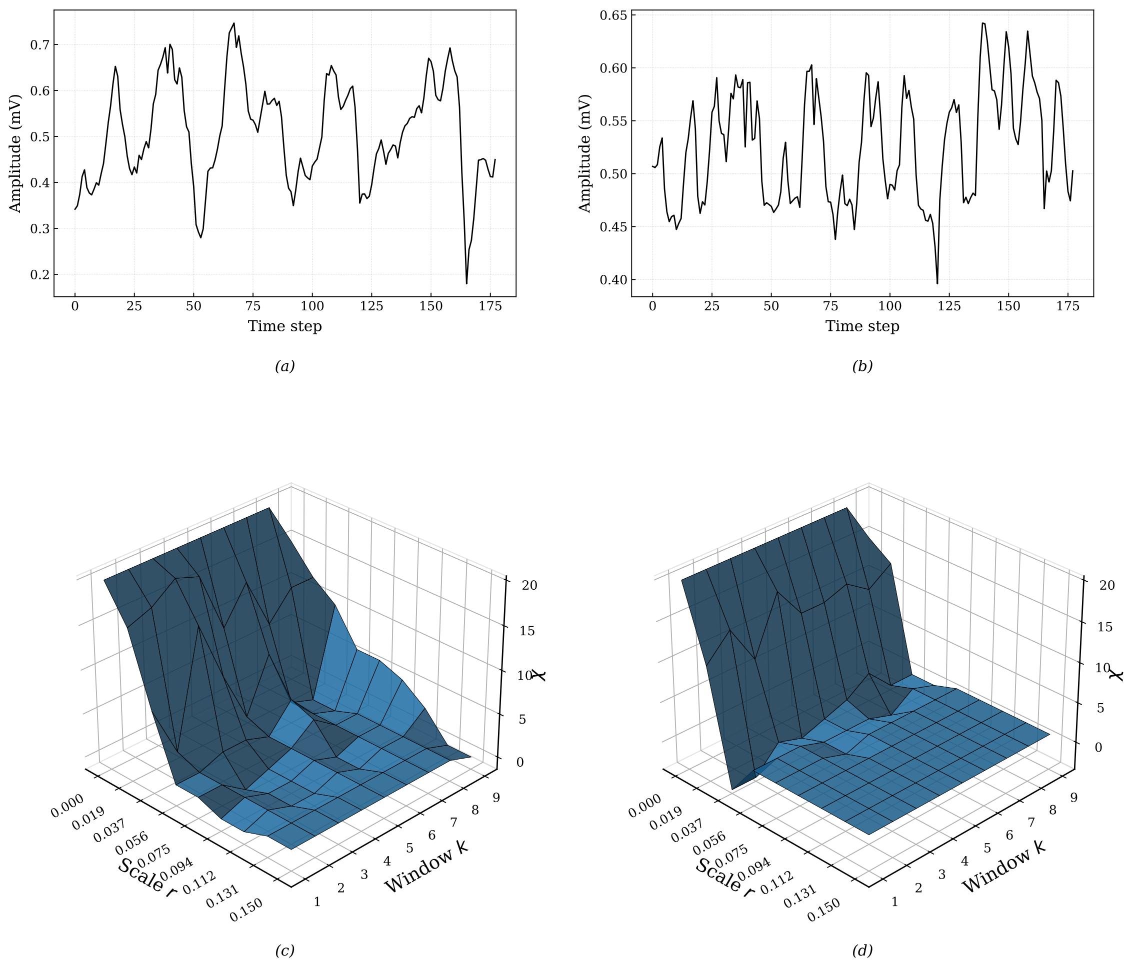

Figure S7: Panels (a) and (b) show representative EEG time series for the seizure and non-seizure classes, respectively. Panels (c) and (d) show the corresponding ECSs.

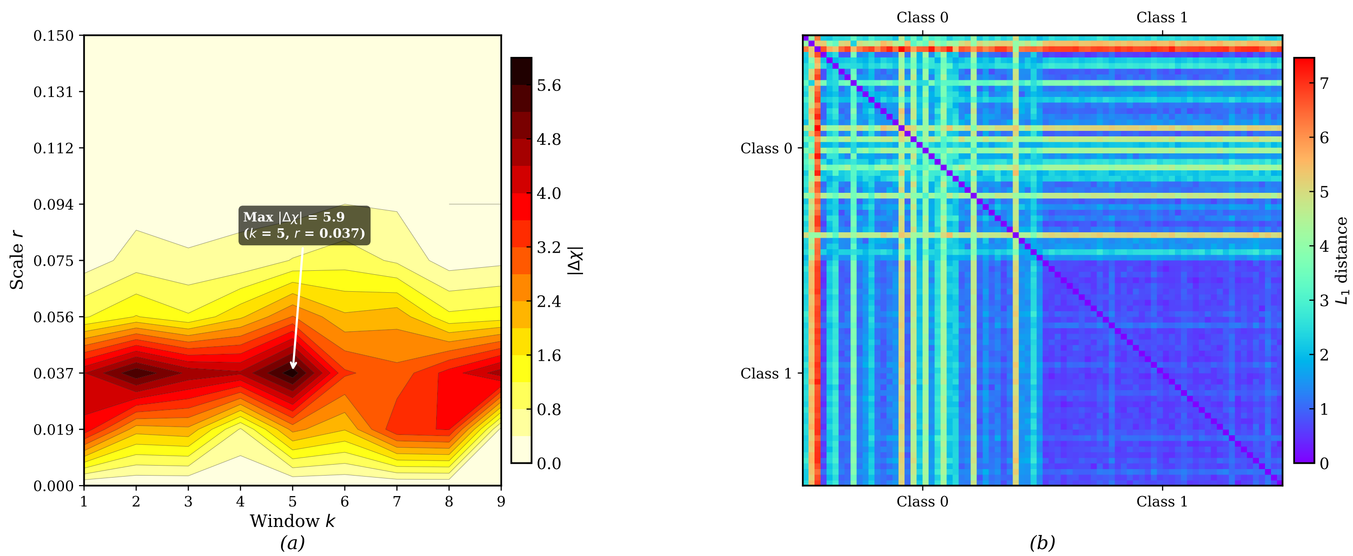

Figure S8: Topological comparison of ECS representations from the *Epilepsy2* training set. Panel (a) shows the point-wise absolute difference $|\Delta\chi|$ between the ECS of each class over the scale–window grid. Panel (b) shows the pairwise L_1 distance between the ECSs of all training samples, displayed as a heatmap.

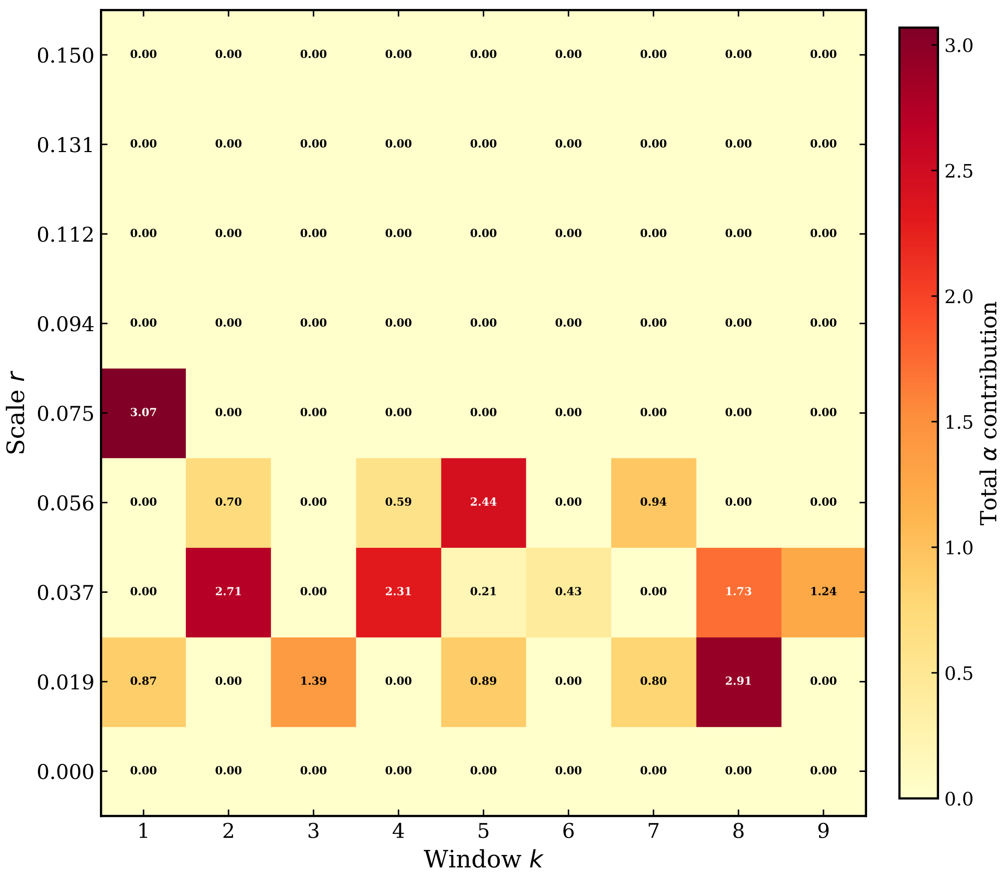

Figure S9: Heatmap of the total α contribution of each ECS feature in the AdaBoost ensemble trained on the *Epilepsy2* dataset (9×9 grid, $T = 81$ stumps).